



PCCP

A new non-diffusional gas bubble production route in used nuclear fuel: Implications for fission gas release, cladding corrosion, and next generation fuel design

Journal:	<i>Physical Chemistry Chemical Physics</i>
Manuscript ID	CP-ART-09-2019-005363.R1
Article Type:	Paper
Date Submitted by the Author:	02-Dec-2019
Complete List of Authors:	Schwantes, Jon; Pacific Northwest National Laboratory, Bair, Jacob; Pacific Northwest National Laboratory Buck, Edgar; Pacific Northwest National Laboratory, Energy and Environment Directorate Devanathan, Ram; Pacific Northwest National Laboratory, Energy and Environment Directorate Kessler, Sean; Pacific Northwest National Laboratory Lach, Timothy; Pacific Northwest National Laboratory Lonergan, Jason; Pacific Northwest National Laboratory McNamara, Bruce; Pacific Northwest National Laboratory Palmer, Camille; Oregon State University, Nuclear Science and Engineering Department Clark, Richard; Pacific Northwest National Laboratory

SCHOLARONE™
Manuscripts

Received 00th January 20xx,
Accepted 00th January 20xx

DOI: 10.1039/x0xx00000x

A new non-diffusional gas bubble production route in used nuclear fuel: Implications for fission gas release, cladding corrosion, and next generation fuel design

Jon M. Schwantes,^{*a} Jacob L. Bair^a, Edgar C. Buck^a, Ram Devanathan^a, Sean H. Kessler^a, Timothy G. Lach^a, J.M. Lonergan^a, Bruce K. McNamara^a, Camille J. Palmer^b, and Richard A. Clark^a

A novel relationship between noble metal phase particles and fission gas bubble production in used nuclear fuel is described. The majority of Te atoms within noble metal phase undergo radioactive decay to form stable Xe within a few hours after particle formation. This results in the production of clusters of Xe atoms contained within the solid metal matrix exhibiting an equivalent gas bubble pressure approaching 1 GPa. These high pressure bubbles are stabilized by the UO₂ within the bulk of the fuel. However, when these bubbles form near the fuel / cladding interface, in combination with local and temporal damage caused by fission recoil, they are capable of overcoming the fracture strength of the UO₂ and rupturing catastrophically. The force of the resulting bubble rupture is sufficient to eject noble metal phase particles several microns into the cladding. This proposed mechanism explains the observance of noble metal phase in cladding and is consistent with a host of morphological features found near the fuel / cladding interface.

Introduction

Noble metal phase (NMP) particles are produced in nuclear fuel during reactor operations¹. They are found throughout used nuclear fuel, have been described as a five metal phase alloy consisting of Ru, Mo, Pd, Tc, and Rh fission products, and are often observed near high pressure gas bubbles that form during irradiation². These particles represent the majority of the undissolved solids that remain following acid dissolution of used nuclear fuel^{3, 4}. They are typically spherical in shape and range in size from a few nanometers to tens of microns in diameter, in which the larger of these particles have been shown to be aggregates of smaller particles^{5, 6}.

The presence of these particles in irradiated nuclear fuel is thought to impart both beneficial and deleterious effects during and after reactor operations^{7, 8}. Hypothesized benefits of NMP particles include enhancing the thermal conductivity of fuel, sequestering and stabilizing semi-volatile fission products (e.g., Tc) thereby minimizing their potential release in the event of cladding failure⁶, facilitating catalytic degradation of H₂O₂ build-up due to radiolysis, and promoting galvanic reduction of U(VI) to U(IV)⁸ - thereby retarding potential migration in the environment after long-term disposition as radioactive waste. Deleterious effects of the formation of NMP particles described in the literature are mostly related to the creation of point and line defects that ultimately lead to cracking and loss of structural integrity of the fuel^{2, 9, 10}. These defects also provide obvious aggregation sites for the accumulation of gas (hydrogen, tritium, Kr, and Xe) generated during fission², although this relatively simple symbiosis between particle and gas bubble formation does not seem sufficient to explain the

^a Pacific Northwest National Laboratory, Richland, WA 99352.

^b Nuclear Science and Engineering Department, Oregon State University, Corvallis, OR 97331.

*Corresponding Author: Jon.Schwantes@pnnl.gov, +1-509-375-7378

presence of relatively high pressure (GPa) gas bubbles in close proximity to NMP particles that have been observed and reported in the literature¹¹⁻¹³.

Four recent works by Pellegrini et al.⁴, Kessler et al.¹⁴, Clark et al.¹⁵, and Buck et al.¹⁶ have dramatically added to the current understanding of the formation and behavior of NMP particles in used nuclear fuel. Pellegrini et al.⁴ recently published the most comprehensive elemental and isotopic analysis of NMP available in the literature to date. Their efforts uncovered a "sixth" fission product element, Te, making up these particles. In addition, they concluded that NMP particles account for on average 36-67%, and as much as 100%, of the total fission product inventory of Ru, Mo, Rh, Pd, Tc, and Te, highlighting the importance of these small species in used nuclear fuel.

states at temperatures (e.g., 505°C) well within the operating temperatures of a typical nuclear reactor, providing a means for transport and formation within the solid UO₂ matrix of nuclear fuel, leading one to conclude that they are candidates as the presumptive seed nuclei for the NMP particles, upon which the other elements making up those particles (Ru, Rh, Mo, and Tc) can grow. Figure 1 provides an example of the fractionation that was first described by Clark et al.¹⁵. Clark et al.'s observations and Kessler's hypothesis of a PdTe seed nuclei are consistent with Devanathan et al.¹⁷ and Jiang et al.,¹⁸ that report Pd being the first of the NMP elements to form within a few hours after the initiation of ion irradiation experiments on CeO₂ doped with Pd, Re (stable analog for Tc), Mo, Ru, and Rh. Finally, Clark et al.¹⁵ reports the presence of NMP particles in the Zr cladding of

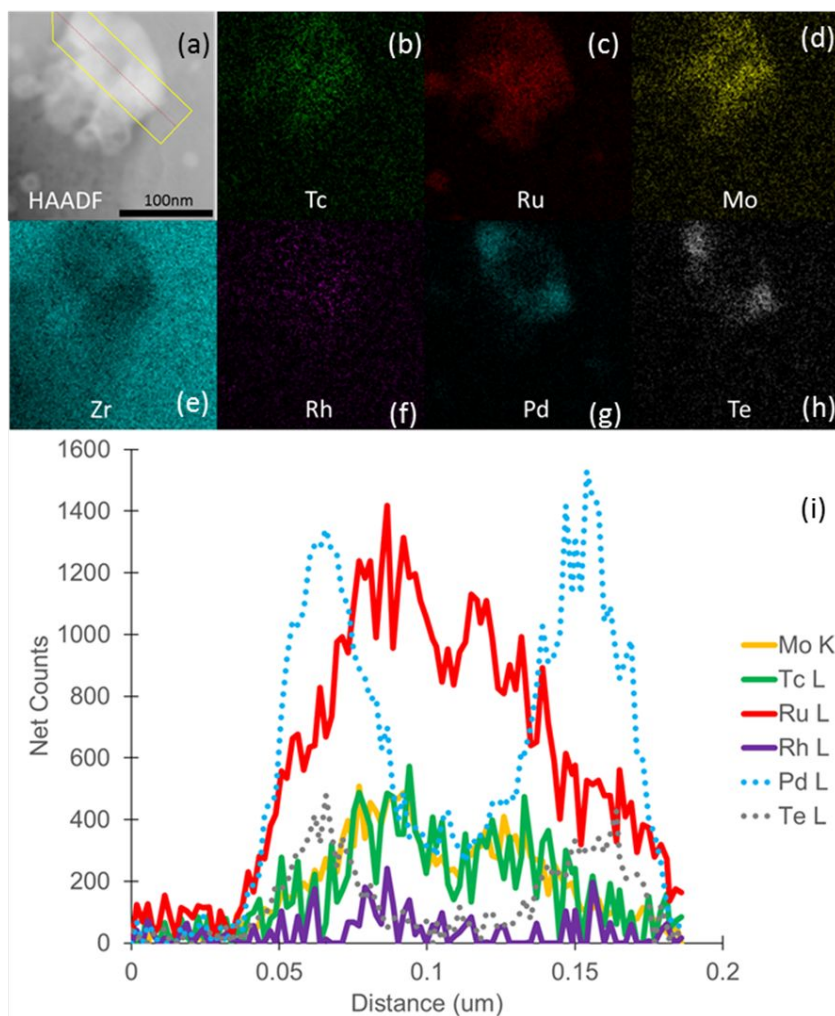


Figure 1(a) High Angle Annular Dark Field (HAADF) image of the interior area of a NMP particle. EDS elemental maps of (b) Tc, (c) Ru, (d) Mo, (e) Zr, (f) Rh, (g) Pd, and (h) Te. (i) Elemental values of Ru, Pd, and Te across the path of the line scan, normalized by total elemental signal (including Tc, Ru, Mo, Zr, Rh, Pd, and Te). Fractionation of PdTe was observed in all NMP particles analysed.

In concert with Pellegrini's discovery of Te as a major component of NMP particles, Clark et al.¹⁵ published experimental observations of the partitioning of Te within these particles, while Kessler et al.¹⁴ provided a thermodynamic basis to explain that discovery. Kessler et al. concluded that the formation of PdTe or similar species was more thermodynamically favorable than that of Pd high entropy alloys of Mo and Ru. These telluride phases also had liquid

fuel, but does not elaborate on whether these particles formed in place or migrated there after the fact.

Using a combination of experimental observations and results from both neutronics simulations and physics continuum modelling borrowed from the ballistics community, we attempt to pull the shroud from some of the mystery surrounding NMP particles: their association with several important fission products; their relationship to high pressure fission gas bubbles

in used nuclear fuel; and potential mechanisms driving the migration of NMP particles into the cladding.

Experimental

ATM-109 Used Nuclear Fuel

The fuel used for this investigation was Approved Testing Material (ATM)-109, a spent fuel from a GE 7x7 BWR fuel irradiated in the Quad Cities 1 reactor between February 1979 to September 1987 and between November 1989 and September 1992. The process history of ATM 109 is not well documented but is believed to be between 65-80 MWd/kgU. Here we have assumed a median value of 70 MWd/kgU to represent the burnup of ATM-109, which provides an average power of 16.7906 MW/MTU. The original uranium oxide (UO₂) fuel was fabricated by the General Electric Company. The UO₂ had an initial 3.0% ²³⁵U enrichment and an initial grain size of ~30 μm. We have previously reported on the nature of the metallic NMP particles from these fuels by dissolving the fuel^{4, 6}. As of July 2018, the ATM-109 fuel had been cooling for approximately 26 years. The material examined in this study included a fragment of cladding and a full-cross section of the ATM-109 fuel. This work concentrated on examining the fuel-cladding interaction zone.

SEM Characterization

Initial surface examinations using Scanning Electron Microscopy (SEM) - Energy Dispersive x-ray Spectroscopy (EDS) were performed using an FEI (Hillsboro, OR, USA) Quanta 250FEG™ field emission gun (FEG)-SEM. The fuel cross section was embedded in a resin and polished to a metallographic finish. Samples were polished to a mirror finish using colloidal silica polishing medium. The SEM was used to locate regions of interest in the metal matrix microstructure. To minimize the effects of sample drift, a drift-correction mode was used during acquisition of the elemental maps. The samples were coated with carbon and imaged at 20 kV, spot size 6, using BSE imaging. The same imaging conditions were used for mapping.

Preparation of TEM Specimens

The SEM mounts were placed in custom metallic holders to reduce the dose during handling with incorporated row-holders and introduced into a FEI Helios 660 NanoLab™ field emission gun (FEG) dual beam focused ion beam/scanning electron microscope (FIB-SEM). This instrument was equipped with an EDAX (EDAX Inc., Mahwah, NJ) compositional analysis system at the Pacific Northwest National Laboratory's (PNNL) Radiological Microscopy Suite in the Radiochemical Processing Laboratory (RPL). The FIB was used to prepare thin foil specimens of dimensions on the order of 15 × 10 μm, with sufficiently low radioactivity levels that they could be analyzed safely in the TEM. A Gallium ion source was used after C and Pt were deposited to minimize the damage from the ion bombardment. Even so, some curtaining was unavoidable. During specimen preparation, the current and accelerating voltage of the ion beam were adjusted from 100 pA to 30 nA and 2–30 kV, respectively, depending on the progress of the thinning operation. Additional thinning of each lift-out was conducted by

an ion beam operating at 2 kV before removal from the sample chamber once these specimens were attached to a Cu TEM half-grid. Very low voltage during this final thinning stage ensures that the potential effects of Ga-ion beam damage on ZrO₂ as reported in the literature is kept to a minimum^{19, 20}. A standard lift-out approach was used to obtain cross-sectional regions²¹.

ORIGEN Model Calculations

The 'activation' mode of ORIGEN was used to simulate the activation and decay of the Te isotopic distribution at early to late times into the operating life cycle. These simulations assumed an average power of 16.79 MW/MTU and only considered activation of the target material, ignoring the production term from fission. The distribution of Te isotopes used as the activation target were predicted using the normal mode of ORIGEN production and depletion at 0.5min, 2 min, 5 min, 60 min, 10 hrs, 100 hrs, and 1000 hrs into the fuel's life cycle. Isotopic results of the 'activation' mode of the Te targets were generated for Te as well as the decay products I, Xe, Cs and Ba for the first and final ATM 109 ORIGEN cycles.

Ballistic Model

Based on the plume of UO₂ material in the ZrO₂ layer, it was decided to model the NMP particle puncture in a similar fashion as has been done previously for ballistic penetration²²⁻²⁹. Due to the complexity of modelling ballistic penetration, the two primary analytical approaches that have been used are energy balance and conservation of momentum. In this case, we chose to implement an energy balance approach. The first step was to define the change in energy, dU , corresponding to the change in displacement, dx , and the force exerted, F , on the NMP particle as shown in Equation 1.

$$dU = -Fd x \quad (1)$$

The mathematical treatment of the forces resisting motion are strongly dependent on the velocity of the projectile and the strain rates experienced by the material being impacted³⁰. Due to this, we have chosen to break the model into two regimes based on the projectile velocity, the first being high speed penetration. In this regime the projectile was going fast enough to strike the target with a force far exceeding its material strength. In this case, the target was considered a fluid without material strength, so it is appropriate to use Bernoulli's equation for the pressure in a fluid to derive the drag force resisting motion³¹. Thus, the drag force was a function of the density of the fluid, ρ_t , the cross sectional area, A , the velocity of the projectile, v , as well as the drag coefficient, C_d , as shown in Equation 2.

$$F_d = -\frac{1}{2}C_d A v^2 \rho_t \quad (2)$$

Plugging Equation 2 into 1 gives the following energy expression

$$dU = -\frac{1}{2}C_d A v^2 \rho_t dx \quad (3)$$

Assuming the projectile energy is entirely due to kinetic motion, the velocity term can be substituted by following expression,

$$v = \sqrt{\frac{2U}{m}} \quad (4)$$

which gives Equation 5.

$$dU = -C_d A \left(\frac{U}{m} \right) \rho_t dx \quad (5)$$

Realizing that this is a differential equation for exponential decay, we arrive at the following solution for the high speed regime.

$$U(x) = U_0 \exp \left(-C_d \left(\frac{A}{m} \right) \rho_t x \right) \quad (6)$$

To solve Equation 1 for low speed ballistic penetration, the material strength of the object being struck must be considered. In this case, the critical parameter is the yield strength, σ_y , of the target materials. This is equivalent to the pressure that must be exhibited by the projectile to strain the material past the elastic limit and cause permanent deformations and break molecular bonds within the target. In the case of a projectile passing through a thick target, the projectile must also compress the material in front of it and to the sides to allow room to pass. This is known as the cavity stress, which is roughly 3 times the yield strength and is equivalent to the force exerted over a unit area as shown in Equation 7^{32, 33}

$$\sigma_c = \frac{F}{A} \quad (7)$$

Equation 7 can be solved for force and plugged into the expression for the change in the system energy, Equation 1, in order to obtain the following expression

$$dU = \sigma_c A dx \quad (8)$$

This is a linear equation and can be solved for the penetration depth, as shown in equation 9

$$x_p = \frac{U}{A \sigma_c} \quad (9)$$

The initial energy from the bubble rupture can be derived from an isothermal expansion of an ideal gas where Q represents heat and W represent work.^{34, 35}

$$Q - W = \Delta U \quad (10)$$

Where ΔU is defined as

$$\Delta U = \int C_v dT \quad (11)$$

For an isothermal process, $dT = 0$, Equation 11 equals zero and equation 10 reduces to

$$W = Q \quad (12)$$

Work can be defined as follows

$$W = \int P dV \quad (13)$$

where P is pressure and V is volume, or, using the ideal gas law, may be redefined as follows

$$W = nRT \int \frac{dV}{V} \quad (14)$$

Integration of Equation 14 results in the following expression.

$$W = nRT \ln \left(\frac{V_2}{V_1} \right) \quad (15)$$

Finally, for an isothermal system, the relation $P_1 V_1 = P_2 V_2$ can be used to substitute V for P and arrive at the final equation for the initial energy of our ejected particle.

$$W = nRT \ln \left(\frac{P_1}{P_2} \right) \quad (16)$$

The drag coefficient is a dimensionless proportionality constant that relates the hydrodynamic force vector of a body in a liquid to a reference area, A , and velocity, v . In practice, the drag

coefficient is typically calculated using relations that depend on the Reynolds number as shown below^{36, 37}.

$$Re = \frac{vL\rho}{\mu} \quad (17)$$

Here, the drag coefficient was calculated based on the following relationship

$$C_d = \frac{24}{Re} \quad (18)$$

The prediction of the NMP particle puncture distance was fairly straight forward but involved several steps.

The first step was to calculate the initial rupture energy and predict the ejection velocity of the NMP particle. This was done using Equation 16 with the assumption that P_2 was equivalent to the cavity stress for the projectile and P_1 was equal to atmospheric pressure. It was assumed to be the operational temperature of the reactor, a broad range of values were used to determine the effect of temperature change on penetration depth. The yield stress of UO_2 has been shown to be a linear function of Young's modulus. Predictions of this function, in turn, are a function of temperature, burnup, and porosity^{38, 39}. Yield stress of UO_2 was thus calculated based upon these works as a function of temperature, burnup and porosity.

The second step was to determine the velocity/energy that marked the boundary between high speed and low speed ballistic puncture. There is no fixed boundary energy or speed that applies to all applications and to the authors' knowledge no mathematical expression has yet been developed to determine this value. Absent of experimental measurements of this value, we use a value of 10 m/s based on general observations in similar systems²²⁻²⁹,

Step three involved the calculation of the energy of the particle through each subsequent material layer. If the final energy was greater than zero, then this value was taken as the initial energy for the next material layer. The material properties used for

Table 1 Ballistic model constants and assumptions.

each layer can be found in Table 1. Due to the high velocities of

Material	Property	Value	Ref
UO_2	Density (300K) (g/cm ³)	10.25	20
	Density (3000K) (g/cm ³)	8	19
	Yield Strength (MPa)	480-568	17-18
	Thickness (μ m)	1.3	Measured
ZrO_2	Pore Diameter (nm)	1200	Measured
	Density (300K) (g/cm ³)	5.87	21
	Density (3000K) (g/cm ³)	5.5	19
	Yield Strength (MPa)	248	21
Fission Particle	Thickness (μ m)	10	Measured
	Density (300K) (g/cm ³)	10.25	Calculate
	Diameter (nm)	200	Measured
Constants	Ideal Gas Constant (J mol ⁻¹ K)	8.314	NA
	High/Low Speed Transition Velocity (m/s)	10	Calculate
	Atmospheric Pressure (MPa)	0.101	NA

the projectiles, and the assumption that the materials behaved as a liquid in the high velocity regime, densities of both UO_2 and ZrO_2 were chosen to be that of a melt at 3000K⁴⁰. If the final energy reached zero in a given layer, then the total distance travelled in both the high and low speed regimes was calculated and the total distance travelled was reported.

Conceptual models of two systems simulated here, one excluding the effects of fission recoil on material strength and the other including these effects, are provided in Figure 2. A list of symbols can be found in Table 2.

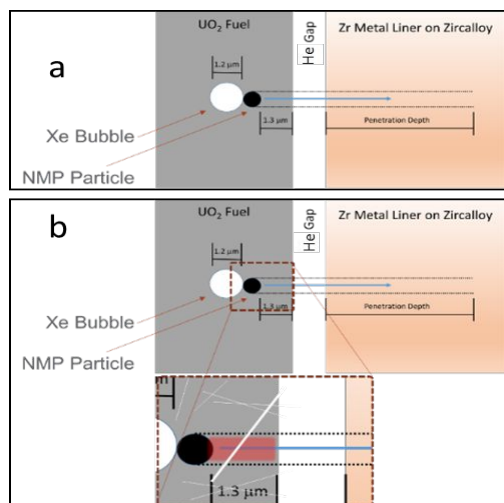


Figure 2 Two conceptual models of systems simulated using the simplified ballistics model: (a) excluding effects of fission recoil on material strength and (b) including these effects.

Symbol	Description	Units	Symbol	Description	Units
U	Energy of the system	J	W	work	J
F	Force	N	ΔU	Change in Total Energy	J
X	Distance	m	C_p	Molar heat capacity	J/(mol-K)
ρ_f	Density of fluid	g/m ³	T	Temperature	K
A	Cross-sectional area	m ²	P	Pressure	Pa
v	Velocity	m/s	V	Volume	m ³
C_d	Drag coefficient	-	n	Number of atoms	-
F_d	Drag force	N	R	Ideal gas constant	J/(mol-K)
m	Mass	g	Re	Reynold's number	-
σ_y	Yield strength	Pa	L	Characteristic length	m
σ_c	Cavity strength	Pa	Y	Young's modulus	Pa
x_p	Penetration depth	m	μ	Dynamic viscosity of fluid	kg/(m-s)
Q	Heat	J			

Table 2 List of symbols.

Results

Detection of Xe, Cs, and Ba in close proximity to NMP Particles

Xenon is the most common fission product generated in spent nuclear fuel but can only be observed by TEM in regions of material where the sample is sufficiently thick to prevent its instant release. Thomas et al.⁴¹ analyzed Xe in fission gas bubbles in UO₂ fuels and determined that the gas must be under high pressure given the concentration and volume occupied by the species. By using a higher energy electron beam (i.e., 300 keV), it was possible to examine the thicker locations in the TEM foils. In Figure 3, a combination elemental map shows the occurrence of Xe gas located between two lobes of NMP in the oxidized Zr metal layer of cladding of Approved Test Material 109 (ATM-109). The Energy Dispersive x-ray Spectroscopy (EDS) spectrum in Figure 3F, confirms the presence of Xe in this region. This was a thicker region of the specimen and it was not possible to obtain a reasonable Electron Energy Loss Spectrum (EELS) signal. The spectrum suggests a minute amount of Kr may also reside in this region, but detection of this element was at low confidence and so cannot be confirmed. Even so, the maximum ratio of Kr to Xe in this region was estimated from the

EDS spectrum to be less than 0.01. This was well below the predicted ratio of ~ 0.05 using ORIGEN calculations, suggesting the mechanisms responsible for the creation of this gas bubble primarily involved Xe atoms.

An additional EDS map of the area surrounding another NMP particle also shows the presence of Cs and Ba (Figure 4), likely decay products of Xe. All of these elements, Xe, Cs, and Ba, were found near the edge of a NMP particle. The discoveries of Xe, Cs and Ba in close proximity to NMP represent the third, fourth and fifth detections of a chain of elements generated from the decay of Te, now known to play an important role in the

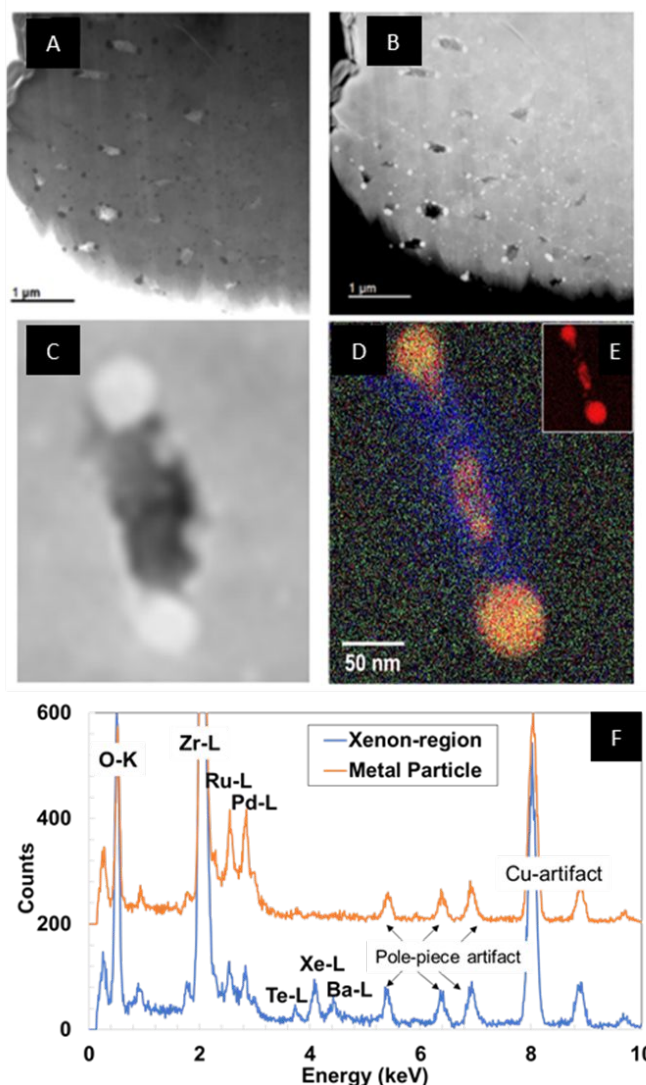


Figure 3(A) Bright Field (BF) and (B) High Angle Annular Dark Field (HAADF) images of "dumb bell" NMP particle morphologies within ZrO₂ layer of cladding on ATM-109. (C-E) Transmission electron image of two NMP particles (yellow and red) connected by a gas bubble (blue) in cladding of ATM-109 fuel. (F) EDS of the NMP particles and the void space between them shown in figures C and D detect the presence of Xe, Te and Ba (partially augmented from Clark et al.¹⁵).

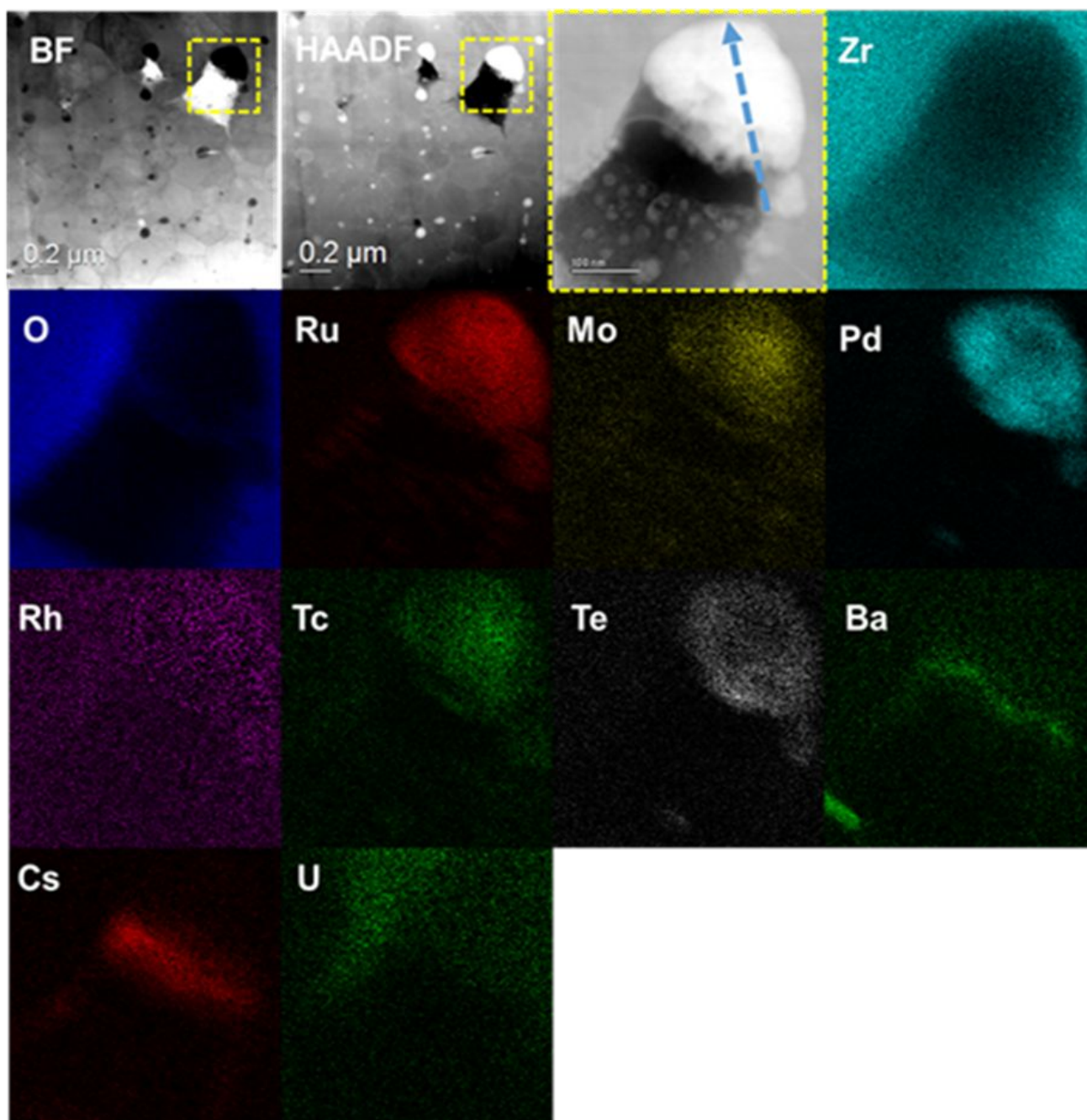


Figure 4 Bright Field (BF) and High Angle Annular Dark Field (HAADF) images of a NMP particle in the cladding of ATM-109 showing the presence of Cs, and Ba, along with Te. Notice that the location of Cs and Ba appear to be on the outer edge of the boundary of the NMP (partially augmented from Clark et al.¹⁵).

formation of these particles. However, each of these elements are also fission products of ^{235}U and ^{239}Pu in their own right. So, it is not immediately clear which of these elements were generated directly by fission and which were generated by a combination of activation and decay. The answer to this question is worth exploring for clues to the formation and behaviour of NMP particles in used fuel.

Discussion

The Relationship between NMP Particles and Locally Produced Xe Gas Bubbles

While Pellegrini et al.⁴ were the first to observe Te within NMP particles, Kessler et al.¹⁴ were the first to suggest that Te as PdTe might play an important role in the formation of NMP particles. A bold assertion considering that, while Te had been detected within NMP particles from three different nuclear fuels, each of these fuels had been cooling for roughly 30 years following their removal from the reactors⁴. In other words, was it Te playing a role in the formation of NMP particles or was it another element that subsequently transmuted to observable quantities of Te via

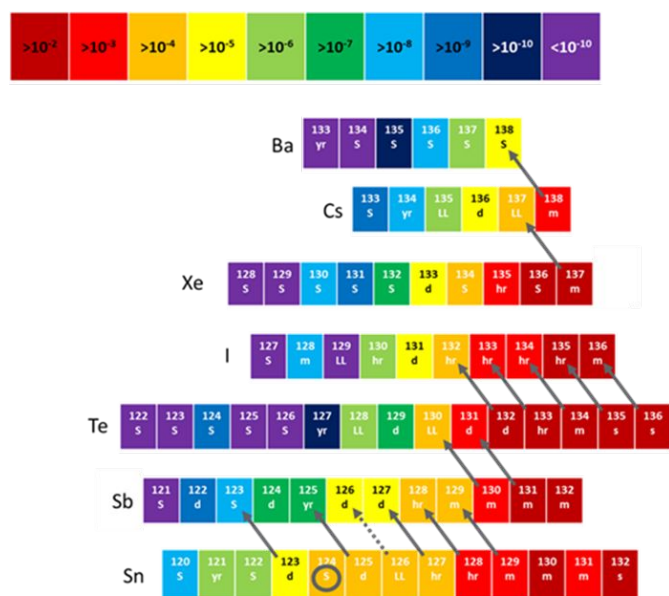


Figure 5 Decay scheme of importance to NMP particles. Color codes represent the independent fission yields from thermal ^{235}U fission. The initiation point of the arrows identify the isotope with the highest independent fission yield of that mass chain. The chart is color coded to show independent fission yields from thermal ^{235}U fission. Arrows indicate the isotope within the mass chain having the highest independent fission yield. Half-lives of each of these isotopes are generally categorized in the range of seconds (s), minutes (m), hours (hr), days (d), years (yr), 1000's of years (long-lived or LL), or stable (S).

decay and / or activation that participated in the formation of these particles? The relationship between NMP particles and other fission product elements detected nearby (I, Xe, Cs and Ba) further complicate efforts to reconstruct the chemistry of these particles at the time of their formation. A portion of the chart of the nuclides applicable to NMP chemistry is shown in Figure 5. While this figure greatly simplifies the actual interplay of fission, activation and decay that ensue during reactor operations, one can generally discern a few key points. First, fission production of Te feeds the mass chains 132-136. Second, most of the other high ($>10^{-2}$ barns) independent fission yield mass chains (i.e., 128-131), while not initiated by Te, decay into longer-lived Te isotopes within minutes to hours after fission production. The timing of this production via decay is important as it is consistent with the likely timeframe over which NMP particles are thought to form. While the exact precipitation rate of NMP particles is unknown, synthetic ion irradiation studies on CeO_2 may provide some idea of the rates of formation of these particles in UO_2 during reactor operations. Recall Devanathan et al.¹⁷ and Jiang et al.¹⁸ observed a Pd-rich particle form within hours after the start of an ion irradiation experiment on CeO_2 doped with NMP elements designed to mimic reactor operations. The two observations suggest that Te would dominate the chemical behavior of this system of elements over a period of minutes, to hours, to days, following fission events and supports the hypothesis by Kessler et al. that Pd in the form of PdTe may play an essential role in the formation of NMP particles. A third takeaway from Figure 5 is that most of the high fission yield mass chains (i.e., 128, 130-134, and 136) dominated by Te would rapidly accumulate as stable or long-lived Xe isotopes. The importance of this point

will be made clear later in this text. While not shown here, a similar trend arises when comparing independent fission yields from thermal ^{239}Pu as well.

Comparing independent fission yields as shown in Figure 5 qualitatively illustrates that I, Xe, Cs and Ba found near NMP particles are from the subsequent decay of Te isotopes that originally participated in the formation of these particles. To develop a more quantitative understanding of the relationship between NMP and the decay products of Te, however, we need to turn to depletion code predictions.

Over short timeframes after reactor startup, the rate of production of Pd and Te from fission becomes relatively constant. This situation leads to a steady-state relationship between fission production of Te and Pd and precipitation of PdTe phase, the presumptive start of the formation and growth of NMP particles. While the rate of precipitation of these particles is unknown, we propose that the process essentially "locks in" a certain abundance of Te isotopes that is unique and separate from that of the average Te isotopic distribution within the bulk of the fuel. Generally speaking, rapid precipitation rates will favor shorter-lived Te isotopes, while slower precipitation rates will favor longer-lived Te isotopes. For a more quantitative understanding of the consequences of precipitation rates on NMP character we employed production and depletion code simulations using ORIGEN-ARP.

Neutronics modeling of this system using ORIGEN involved a two-step process to first predict the initial Te isotopic distribution within noble metal phases over a range of possible particle precipitation rates, and then simulate the transmutation of Te in those particles due to activation and decay over the operating cycle of the reactor. The first step simulated Te isotopic distributions at discrete times, from 0.05 m to 1000 hr after the initiation of fission. The second step simulated the activation and decay of the Te isotopic distribution generated by the first step using the 'activation' mode of ORIGEN to represent the genesis of Te isotopes within NMP particles over the operating life cycle of the reactor. More details of these simulations are provided in the materials and methods section of this paper.

Depletion code modeling provides a number of findings - some intuitive, some not so intuitive. First, as one might expect, the precipitation rate of the NMP particle has a dramatic effect on the initial isotopic distribution of Te within NMP particles. Figure 6 illustrates this finding, where the relative abundance of Te isotopes shifts towards lighter, more stable, isotopes as a function of increasing precipitation time. Also somewhat intuitive, Te isotope distribution within the NMP, as well as those of its decay products, quickly arrive at meta-stable equilibrium during reactor operations (see Figure 7). For Te, isotopes at mass numbers 128 and 130 remain essentially unchanged from their initial values during reactor operations, while isotopes at the other mass numbers quickly drop to insignificant values due to decay. These simulations predict that ^{128}Te would be depleted relative to ^{130}Te when compared with their average composition within the bulk fuel. This prediction is qualitatively consistent with results reported by Pellegrini et al.⁴ in which Te isotopic abundances within NMP particles were compared with ORIGEN predictions of bulk average fuel

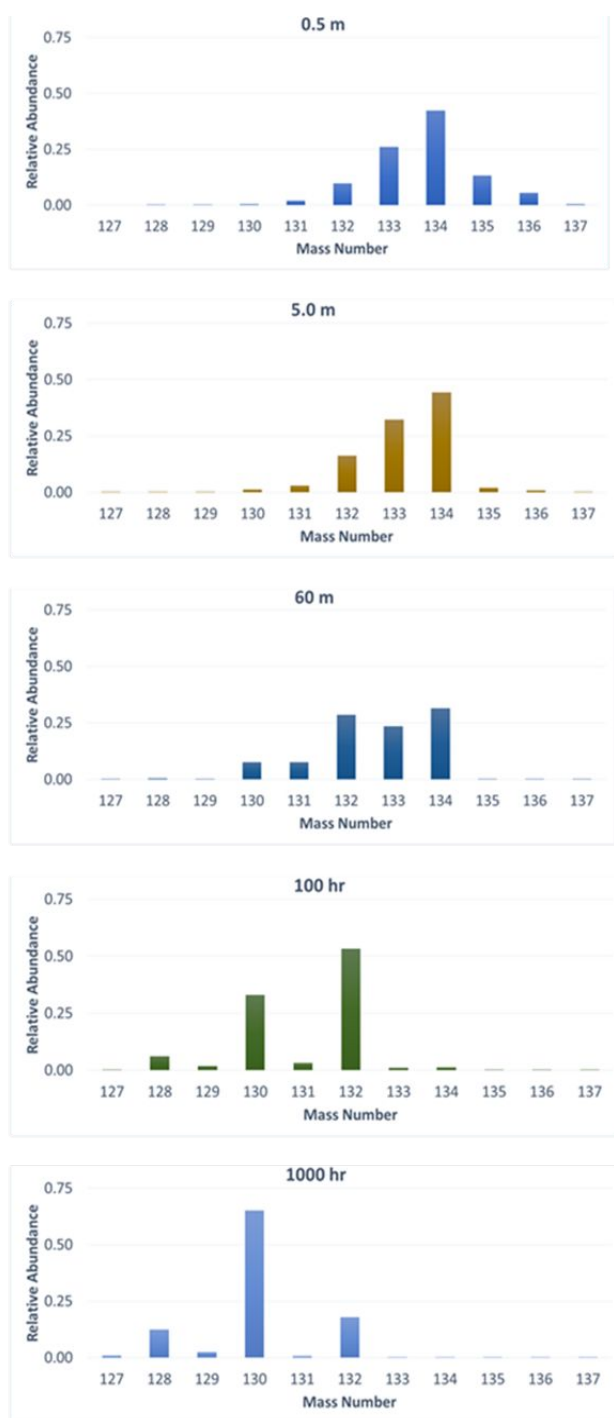


Figure 6 Predicted Te isotopic distribution within NMP particles as a function of precipitation times.

composition. One rather surprising result from these simulations is the effect on the production of the daughter products of Te associated with NMP particles. A more rapid precipitation rate of NMP particles resulted in particles being enriched in the heavier, shorter-lived, isotopes of the element. This, in turn, means a greater fraction of the total Te mass in these particles decay over time to form I, Xe, Cs, and Ba isotopes. Figure 8, illustrating this point, shows the relative abundance of decay products of Te in NMP particles (normalized by the Te mass loss due to decay) as a function of precipitation time of those particles. Also shown, the fraction of Te mass remaining after metastable equilibrium as a function of precipitation time. Figure 8 shows that for precipitation times of an hour or less, about 90% of all Te atoms in NMP particles will decay to form I, Xe, Cs and Ba. Most of those decays end up as stable Xe, with roughly 70 atoms of Xe produced for every 100 atoms of Te that decay. Xe production from Te in NMP, however, does not drop dramatically with precipitation time unless precipitation occurs over a duration of 100 hours or more. The structure that would ensue following Te decay within a NMP particle would essentially create a substitutional impurity point defect of its decay products within the structure in a relatively short period of time following precipitation. The Xe concentration within PdTe particles formed at different precipitation rates over the lifecycle of the reactor is provided in Figure 9. From the figure, Xe concentrations reach a maximum value at roughly a day after fission begins. As Xe atoms accumulate within the PdTe phase, eventually Xe atoms will interact and form clusters. The primary means for migration of Xe atoms within a solid matrix will be via the diffusion of vacancy defects, which should be present to a great extent as a result of radiolysis and fission recoil. Xe concentrations will be on the order of solid matrix densities, which, if present as a gas, would reach GPa pressures within the temperature regime of an operating reactor. These predicted pressures are consistent with fission gas bubble pressure measurements reported in the literature¹¹⁻¹³ and summarized in Table 3.

The formation, growth and migration of fission gas bubbles have been the subject of much research within the literature due, in large part, to the role they play in the loss of integrity of nuclear fuel during reactor operations⁴². Gas bubble formation during irradiation causes swelling⁹ that can lead to cracking and increases porosity, which has been shown to account for the majority of the loss of material strength in UO₂³⁸.

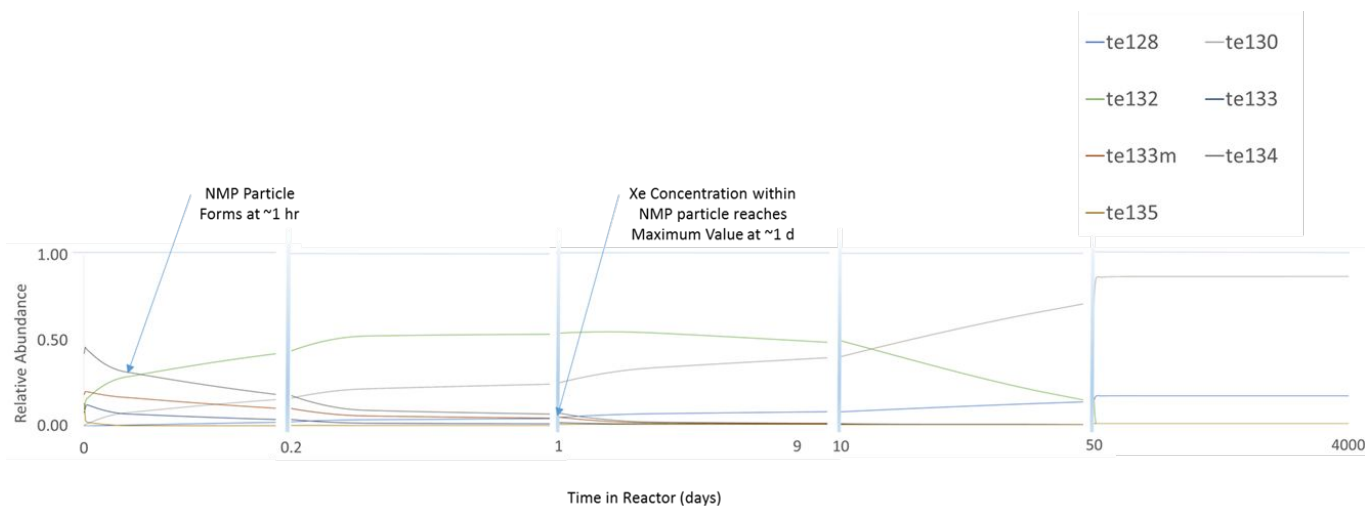


Figure 7 Distribution of Te isotopes 128-137 as a function of time in reactor for ATM-109. Figure shows most of the key isotopes reaching metastable equilibrium within 50 days.

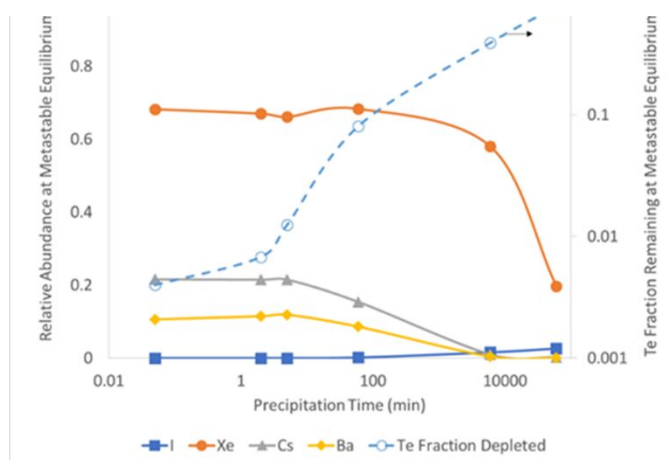


Figure 8 Relative abundance of Te decay products (normalized by the Te mass loss due to decay) within NMP particles as a function of precipitation time. Model results collected after metastable equilibrium is reached after reactor start up. The dashed line and secondary y-axis shows the fraction of Te remaining as a function of precipitation time.

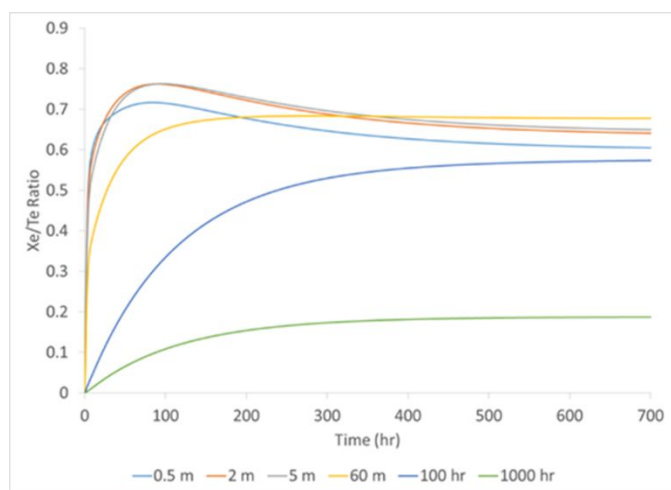


Figure 9. Xe concentrations within PdTe seed particles for NMP particles.

Table 3 Summary of measured Xe gas bubble pressures in used nuclear fuel reported in the literature.

Bubble radius (nm)	Pressure (MPa)	Method	Reference
4-10	1600-15000	TEM	Nogita & Une, 1998
25-40	1000	N/A	Thomas (sited by Nogita & Une, 1998)
600	90-210	N/A	Une et al. (sited by Nogita & Une, 1998)
n/a	15-33	LA-ICP-MS & SEM/EPMA	Horvath, 2008
150-1050	0.2-56.4	SIMS-EPMA	Cagna, 2016
760	45	SIMS-EPMA	Walker, 2009

Xe Gas Bubble Rupture at the Fuel / Cladding Interface

Bubble rupture is an extreme event in which the pressure within a bubble rapidly and catastrophically exceeds the yield strength of the material surrounding the bubble by a factor of three²²⁻²⁴. This value is known as the cavity stress (σ_c) of the material. In instances in which the pressure increase inside the bubble surpasses the yield strength but not the σ_c of the surface material, leaking of gas atoms will ensue without catastrophic failure. Catastrophic fuel failure at the fuel/cladding interface has previously been reported, but only under accident conditions in which the heating rates can approach 10^5 K/s^{43, 44}. In these instances, rapid increases in fuel temperature (much faster than diffusion) drive rapid increases in fission gas bubble pressures (GPa) that lead to an energetic ejection of fine grained fuel fragments at high velocities (10 m/s) at the fuel/cladding interface. However, catastrophic fuel failure affecting cladding integrity at the fuel / clad interface under normal operating conditions would not be expected to progress in this same manner. While the mechanism described by Lamoine et al.⁴⁴ may be valid for such events under reactivity initiated accidents, the level and rate of temperature increase needed to explain this phenomenon would not be reasonable under normal operating conditions like that represented by the

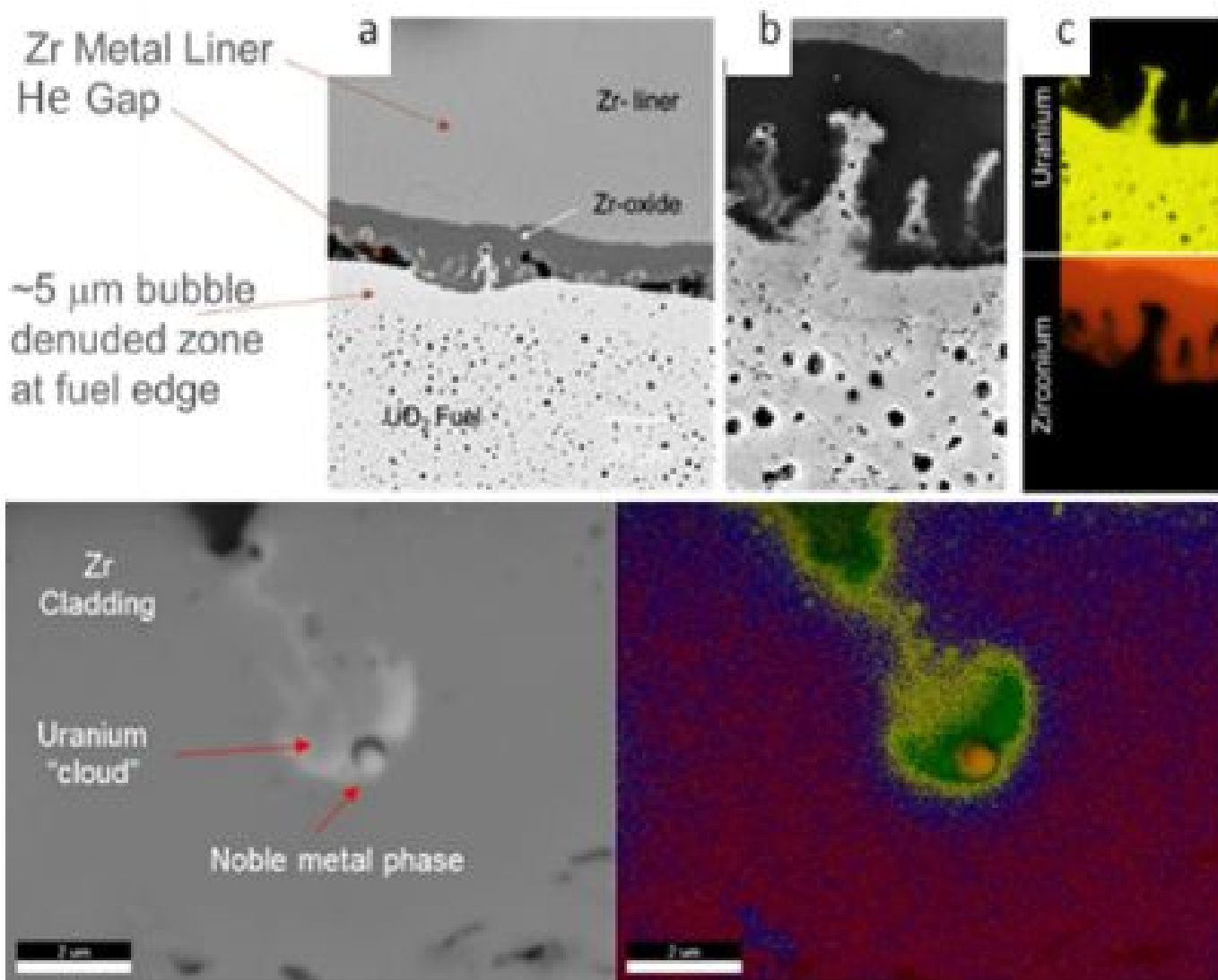


Figure 10 Electron image of fuel / cladding interface of ATM-109 BWR fuel after irradiation. (a) Major features of the interface. (b) high resolution image showing fuel / cladding interaction indicative of high Re numbers turbulent mixing. (c) Elemental map showing the distribution of U and Zr within the mixing zone. (d) Close up images of a NMP particle that has been ejected from the fuel surface into the ZrO₂ layer of the cladding. (e) EDS generated "phase" map showing the NMP in orange, and high concentration of U in green, with a trail of U (yellow) present at lower concentrations. Red and blue colors were dominated by the presence of Zr (partially augmented from Clark et al.¹⁵).

irradiation history of specimen ATM-109 studied here. Nonetheless, observations such as those first reported by Clark et al.¹⁵ and captured in Figure 10 compel us to consider the concept of bubble rupture under normal reactor operations as a possible means for fission gas release at the fuel / cladding interface.

There are several features within Figure 10 that drive the interest to explore the possibility of bubble gas rupture. First, and most obvious, the presence of large gas bubbles within the bulk of the used fuel. Secondly, the bubble denuded zone within a $\sim 5\mu\text{m}$ distance from the outer fuel layer. This distance is roughly equivalent to the migration path length of a fission fragment traveling through UO₂ fuel (Figure 2) during fission recoil. Also, note the presence of a remnant of the Helium gap (1-10 MPa He at startup) in some areas between fuel and cladding. Indications of fuel / cladding interaction and the morphological features that ensue are indicative of high Reynolds numbers and turbulent mixing (conditions that one might expect to occur following a catastrophic event like bubble

rupture) rather than a scenario such as gas seeping from intragranular pores of the fuel – a mechanism that would not be expected to alter the interface significantly. Notice the oxidation of the first $5\mu\text{m}$ or so of the Zr metal protective layer on the Zr-alloy cladding. Lach et al.,⁴⁵ described this region in great detail, noting important phase transitions and grain size differences with distance from the interface. The oxidation of the protective metal layer occurring during reactor operations has been hypothesized by others to result from interactions with high temperature steam⁴⁶, which suggests the cladding had fully breached at some location to allow for the steam to access the inner cladding wall. However, the cladding in this study did not appear to be breached beyond the oxidized metal layer. Finally, notice a closeup image of a NMP particle within cladding near the fuel / cladding interface (Figure 10d and 10e). The appearance of a NMP particle being ejected from the fuel with high concentrations of U surrounding it, while curious, are all consistent with the notion of high pressure bubble rupture

at the interface and beg for a more quantitative assessment of this possibility.

Here, bubble gas rupture at the fuel / cladding interface is investigated using a simple continuum model borrowed from the ballistics community. This model has been described in detail within the methods section of this paper, including important assumptions and constants used for simulating results (see Table 1). A conceptual model of the simulated systems are also provided in Figure 2 for discussion purposes. These conceptual models were based upon observations like those shown in Figure 10. Important dimensions of the fission gas bubble, the mean distance between the bubble and the fuel interface, the NMP particle diameter and the dimensions of the

a relatively inelastic ceramic prone to brittle failure mechanisms. Yield/tensile strength (σ_y) was calculated from the empirical relationship shown in Equation 19, relating it to

Table 5 Ballistic puncture model results for dumbbell shaped morphologies

Material	Cavity Strength (MPa)	Particle Diameter (nm)	Displacement (nm)
Undamaged ZrO ₂	744	50	57
Recoil Damaged ZrO ₂	248	50	125

Young's modulus (Y) as a function of porosity (p) based upon measurements of the two values reported in the literature³⁹.

$$\frac{Y}{\sigma_y} = 205.81 \exp(0.48p) \quad (19)$$

Young's modulus was calculated for UO₂ as a function of p , temperature (T -°C) and burnup (B-GWd/MTU) from Equation

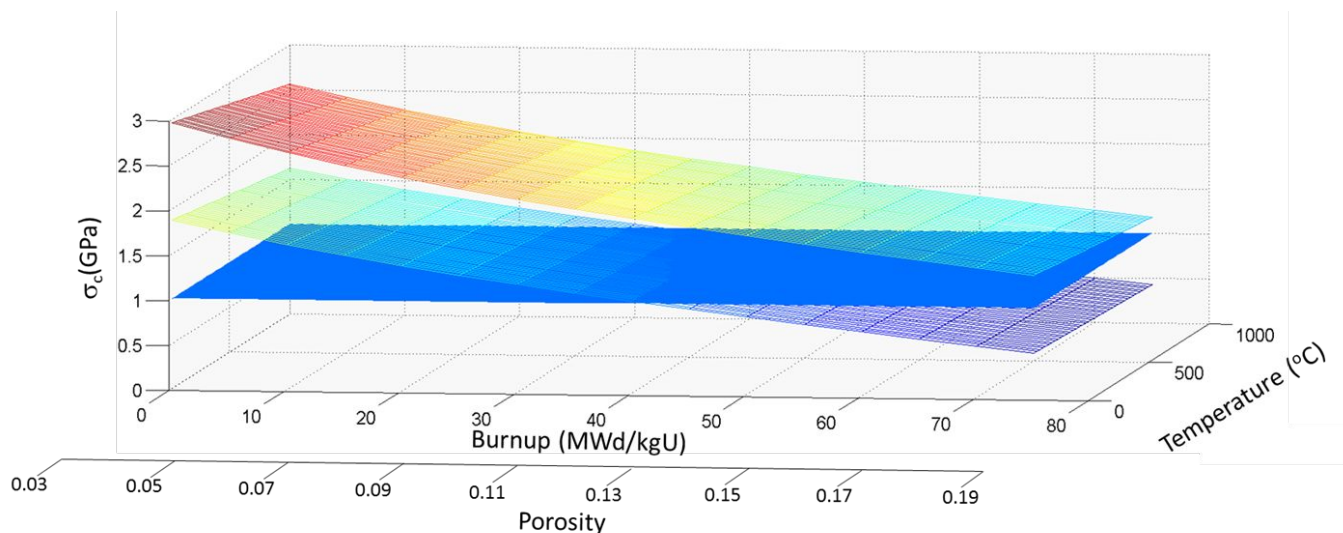


Figure 11 Cavity stress (σ_c) of UO₂ in the bulk and near fission recoil damage as a function of burnup, porosity and temperature. The 1-GPa pressure surface is plotted in the figure for reference.

Table 4. Summary of ballistic puncture model results.

Temperature (°C)	Y UO ₂ (Gpa)	σ_y UO ₂ (Mpa)	Local σ_y UO ₂ (Mpa)	C_d	Particle Rupture Velocity - v (m/s)	ZrO ₂ Penetration Depth - x_p (μ m)
25	117	531	223	0.196	498	3.52
100	116	525	220	0.199	489	3.39
200	114	518	217	0.204	478	3.23
300	112	510	214	0.208	469	3.10
400	111	503	211	0.212	460	2.98
500	109	496	208	0.215	453	2.87
600	107	488	205	0.219	445	2.77
700	106	481	202	0.221	441	2.71
800	104	473	199	0.226	432	2.58
900	103	466	195	0.229	425	2.49
1000	101	459	192	0.233	418	2.41

cladding relative to the fuel interface were all taken from actual observations. Here we test the hypothesis of bubble rupture at the fuel / cladding interface under two scenarios - one in which we exclude local effects of fission recoil on material strength (see Figure 2a) and the other in which we consider these effects (see Figure 2b). Our continuum model is used to describe a bubble gas rupture event in a material weakened by the progressive accumulation of atomic displacement damage from fission recoils.

An important assumption of the continuum model is the value used for the yield strength of UO₂ and ZrO₂. Here, we take the conservative approach of equating yield to tensile strength for

20 taken from the most up-to-date model in the literature by Capia et al.³⁸.

$$Y = 223.7(1 - 2.6p)[1 - 1.394 \times 10^{-4}(T - 20)]\{1 - 0.1(2 - 0)\}$$

In addition to the bulk effects that the irradiation environment has on the value of σ_y , the recoil of fission fragments can also temporarily and locally reduce material strength along the recoil path until annealing is able to re-establish the majority of the original integrity. Yablinsky et al.⁴⁷ quantified this loss of integrity as temporary decrease in density of 13% throughout a ~4-nm diameter cylindrical volume of material along the recoil path. Treating that decrease in density as a corresponding increase in porosity, the effect on σ_c (three times σ_y) was calculated using equations 19 and 20 and summarized in Table 1 and Figure 11.

Results from these calculations, when ignoring temporal effects near fission recoil paths, indicate that catastrophic bubble rupture would not ensue even though the yield strength of the UO₂ would be exceeded by the pressure of a fission gas bubble (Table 4). In this instance, gas would be expected to seep from the bubble without catastrophic loss of material integrity surrounding the bubble and without ejecting the NMP particle from the fuel into the cladding. In the second scenario, however, fission recoils would generate a temporary, localized, reduction of the yield strength of the UO₂ skin between the

bubble and the fuel surface sufficient for a 1GPa gas bubble to exceed the σ_c of the UO_2 and cause catastrophic bubble rupture. In that instance, a 200 nm NMP particle ejected from the fuel by a 1.2 μm gas bubble with a pressure of 1 GPa would be propelled up to $\sim 4 \mu\text{m}$ into the cladding. This predicted depth of penetration is consistent with observations from the literature¹⁵.

The continuum model was also used to investigate rather odd morphologies of NMP particles found within the cladding of ATM-109. Electron images of these “dumb bell” shaped morphologies are provided in Figure 3. Here, we assume interstitial Xe gas generated within the ejected NMP particle accumulated at the intra-granular boundary between two phases (presumably PdTe phase on one side and Ru/Mo/Tc/Rh rich phases on the other) by vacancy defect diffusion or a similar mechanism, consistent with our observations that place Xe, Cs and Ba within the void space between two NMP particles, but not within the interstices of the particle. The intra-granular pressure of Xe within a recently produced NMP particle being ejected into the cladding is assumed to eventually (over the period of ~ 1 day) approach $\sim 1\text{GPa}^{11-13}$ due to Xe production from Te decay. As these NMP particles are ejected from the fuel surface into the ZrO_2 the σ_c for ZrO_2 is eventually exceeded, leading to bubble rupture and relatively symmetric splitting of the NMP particle along the PdTe phase boundary. To test this hypothesis, the continuum model was used to predict the expected separation distance of two half-spheres of a 100 nm NMP particle in ZrO_2 . The NMP particle size was taken from Figure 3, while the bubble size at the PdTe phase boundary within the particle was set equal to the intra-granular space between the two phases sufficient to create a Xe gas pressure of 1 GPa, assuming the pressure of the void space shown within Figure 3 is at equilibrium after rupture. This length was found to be $\sim 10 \text{ \AA}$. A 50nm NMP particle would be expected to generate 10^6 Xe atoms. The continuum model predicts the amount and pressure of the intra-granular Xe gas would be sufficient to separate the NMP particle in two by a distance of between 57-125 nm (see Table 5) within the ZrO_2 , depending upon whether material strength effects due to fission recoil are considered or not. These calculations are consistent with observations shown in Figure 3, suggesting that this hypothesis is a reasonable one. Outcomes from this research have important implications for next generation fuel designs capable of minimizing cladding corrosion and enhancing fuel integrity at higher burnups. The relationship between NMP particles and the production of high pressure gas bubbles, suggests one might be able to alter the latter by manipulating the former for beneficial effects. This approach, for instance, could be used to distribute Xe gas atoms to a greater number of smaller ($\sim \text{nm}$) bubbles, which have a higher likelihood of redissolving (redistributing) back into the UO_2 matrix due to surface effects⁴⁸. These surface effects also allow the surrounding material to withstand higher bubble pressures, so distributing more of the fission gas to smaller bubbles should minimize fuel swelling. Smaller bubbles are also stabilized within the UO_2 matrix by Schottky defects, which limits their migration and therefore their ability to contribute to bubble growth⁴⁸. Near the fuel / cladding interface as well, the

potential energy of a smaller bubble should lower the possibility of and resulting damage from bubble rupture.

Conclusions

A number of recent discoveries related to NMP particles have enhanced our understanding of these particles, their formation, fate and importance within nuclear fuel during reactor operations. These discoveries include:

- 1) The existence of Te, the “sixth” element, in NMP particles⁴
- 2) The observations that the distribution of Te is correlated to that of Pd and anti-correlated to Ru, Mo, Tc and Rh within NMP particles, along with the prediction from thermodynamic calculations that this was likely a PdTe phase, which could become liquid within the operating temperature range of the reactor^{14, 15}.
- 3) The observation that Pd phases are likely the first to form of the NMP elements during synthetic ion irradiation experiments designed to mimic nuclear operations^{17, 18}.
- 4) The discovery of NMP particles within fuel cladding¹⁵.
- 5) The close association of NMP particles with a number of other important fission products including I^{16} , Xe^{15} , Cs (this work), and Ba (this work).

Based upon these findings we make several important conclusions. The nucleation seed for the formation and growth of NMP particles is PdTe or a similar phase. Under most reasonable precipitation scenarios simulated here, the majority of the Te atoms that form the PdTe seed for NMP particles will decay to form stable Xe within roughly one day after particle formation. Local production of Xe from the decay of Te within NMP particles contained within the solid lattice structure of the particle would be at a density equivalent to a fission gas bubble with an internal pressure approaching 1 GPa under typical operating conditions of a reactor. This pressure is consistent with observations from the literature¹¹⁻¹³. Near the fuel / cladding interface, within the range of travel of a recoiling fission product ($< 10 \mu\text{m}$), the pressure of these locally produced Xe gas bubbles is sufficient to catastrophically overcome the yield strength of the radiation damaged UO_2 and rupture. The force of a $\sim 1.2 \mu\text{m}$ diameter bubble rupture is sufficient to drive a 0.2 μm diameter NMP particle roughly 4 μm into the Zr cladding, consistent with observations from the literature¹⁵. Once driven into the ZrO_2 matrix from bubble rupture near the fuel surface, the pressure from these intra-granular Xe bubbles at the PdTe interface is able to split these particles in two and displace these fragments over 50 nm.

These results resolve the long held mystery of the relationship between NMP particles and fission gas bubbles. This relationship is the basis for a novel, non-diffusional, mechanism for the production of high pressure fission gas bubbles in nuclear fuel by the localized decay of Te bound within NMP particles. Near the fuel cladding interface, these bubbles can rupture catastrophically and corrode the cladding surface. These conclusions have far reaching implications on the current understanding of the behavior of fission gas atoms within irradiated nuclear fuel, their mobility or lack thereof, the mechanisms controlling the formation of point and line defects that lead to cracking and loss of fuel integrity, the driving forces

behind fission gas release, cladding corrosion and the science driving next generation of high burnup fuel designs.

Conflicts of interest

There are no conflicts to declare.

Acknowledgements

This work was supported by the Laboratory Directed Research and Development (LDRD): Nuclear Processing Science Initiative (NPSI). Pacific Northwest National Laboratory (PNNL) is a multi-program national laboratory operated for the U.S. Department of Energy (DOE) by Battelle Memorial Institute under Contract DE-AC06-76RLO 1830.

Most experiments were performed in the PNNL RPL Facility within the RPL Microscopy Quiet Suite, which is outfitted with a FEI Helios 660 FIM/SEM and a JEOL GrandARM300 Aberration Corrected (AC) STEM/TEM. Additional TEM/STEM measurements were also collected on a JEOL ARM200 AC-STEM/TEM located in 3410, part of the Physical Sciences Facility. All of these instruments are part of PNNL's Institutional Microscopy Tools.

Notes and references

1. B. T. Bradbury, J. T. Demant, P. M. Martin and D. M. Poole, *J. Nucl. Mater.*, 1965, **17**, 227-236.
2. H. Kleykamp, J. O. Paschoal, R. Pejsa and F. Thummler, *J. Nucl. Mater.*, 1985, **130**, 426-433.
3. B. K. McNamara, E. C. Buck, C. Z. Soderquist, F. N. Smith, E. J. Mausolf and R. D. Scheele, *J. Fluorine Chem.*, 2014, **162**, 1-8.
4. K. L. Pellegrini, C. Z. Soderquist, S. D. Shen, E. J. Krogstad, C. J. Palmer, K. R. Gerez, E. C. Buck, T. G. Lach, J. M. Schwantes and R. A. Clark, *Anal. Chem.*, 2019, **91**, 6522-6529.
5. Y. Cui, Y. Huo, S. Ding, L. Zhang and Y. Li, *J. Nucl. Mater.*, 2012, **424**, 109-115.
6. E. C. Buck, E. J. Mausolf, B. K. McNamara, C. Z. Soderquist and J. M. Schwantes, *J. Nucl. Mater.*, 2015, **461**, 236-243.
7. B. J. Lewis, W. T. Thompson, M. R. Kleczek, K. Shaheen, M. Juhas and F. C. Iglesias, *J. Nucl. Mater.*, 2011, **408**, 209-223.
8. P. Carbol, P. Fors, T. Gouder and K. Spahlu, *Geochim. Cosmochim. Ac.*, 2009, **73**, 4366-4375.
9. D. R. Olander, *Fundamental Aspects of Nuclear Reactor Fuel Elements*, California Univ., Berkeley (USA). Dept. of Nuclear Engineering, 1976.
10. J. H. Guttus, H. Howl and H. Hughes, *Nucl. Appl. Tech.*, 1970, **9**, 40-46.
11. K. Nogita and K. Une, *Nucl. Instrum. Meth. B*, 1998, **141**, 481-486.
12. C. Cagna, I. Zacharie-Aubrun, P. Bienvenu, L. Barrallier, B. Michel and J. Noirot, *IOP Conf. Ser.: Mater. Sci. Eng.*, 2016, **109**, 012002.
13. C. T. Walker, S. Bremier, S. Portier, R. Hasnaoui and W. Goll, *J. Nucl. Mater.*, 2009, **393**, 212-223.
14. S. H. Kessler, T. G. Lach, K. E. Garrett, M. A. Conroy, K. L. Pellegrini, E. C. Buck, D. G. Abrecht, J. M. Schwantes and R. A. Clark, *J. Nucl. Mater.*, Accepted.
15. R. A. Clark, T. G. Lach, M. Conroy, K. L. Pellegrini, E. C. Buck and J. M. Schwantes, *Mater. Degrad.*, Accepted.
16. E. C. Buck, E. J. Mausolf, B. K. McNamara, C. Z. Soderquist and J. M. Schwantes, *J. Nucl. Mater.*, 2016, **482**, 229-235.
17. R. Devanathan, W. Jiang, K. Kruska, M. A. Conroy, T. C. Droubay and J. M. Schwantes, *J. Mater. Res.*, 2019, **34**, 709-719.
18. W. L. Jiang, M. A. Conroy, K. Kruska, M. J. Olszta, T. C. Droubay, J. M. Schwantes, C. A. Taylor, P. M. Price, K. Hattar and R. Devanathan, *J. Phys. Chem C*, 2019, **123**, 2591-2601.
19. H. Berek and C. G. Aneziris, *Ceram. Int.*, 2018, **44**, 17643-17654.
20. F. Baxter, A. Garner, M. Topping, H. Hulme, M. Preuss and P. Frankel, *J. Nucl. Mater.*, 2018, **504**, 176-180.
21. J. Li, T. Malis and S. Dionne, *Mater. Charact.*, 2006, **57**, 64-70.
22. C. E. Anderson, *Int. J. Impact Eng.*, 2017, **108**, 3-26.
23. J. Awerbuch and S. R. Bodner, *Int. J. Solids Struct.*, 1974, **10**, 671-684.
24. B. J. Noonan and H. K. Steves, *The Performance of Small Arms Ammunition When Fired into Water*, U. S. N. O. Laboratory, White Oak, Maryland, 1970.
25. A. Brown, *Int. J. Mech. Sci.*, 1964, **6**, 257-260.
26. B. Paul and M. Zaid, *J. Franklin Inst.*, 1958, **265**, 317-335.
27. M. Zaid and B. Paul, *J. Franklin Inst.*, 1957, **264**, 117-126.
28. W. T. Thomson, *J. Appl. Phys.*, 1955, **26**, 80-82.
29. G. I. Taylor, *Q. J. Mech. Appl. Math.*, 1948, **1**, 103-124.
30. J. A. Zukas, *High velocity impact dynamics*, John Wiley & Sons, Inc., New York, 1990.
31. R. A. Serway, *Physics for Scientists and Engineers*, 4th edition, Saunders College Publishing, 1996.
32. J. D. Clayton, *Def. Technol.*, 2016, **12**, 334-342.
33. J.-F. Lou, Y.-G. Zhang, Z. Wang, T. Hong, X.-L. Zhang and S.-D. Zhang, *Def. Technol.*, 2014, **10**, 239-244.
34. S. S. Paulsen, *Pressure Systems Stored-Energy Threshold Risk Analysis*, Report PNNL-18696, Pacific Northwest National Laboratory, Richland, 2009.
35. M. Coleman, M. Cain, R. Danna, C. Harley and D. Sharp, *A Review of Energy Release Processes from the Failure of Pneumatic Pressure Vessels*, Eastern Space and Missile Center, Patrick Air Force Base, Florida, 1988.
36. H. Yang, M. Fan, A. Liu and L. Dong, *Int. J. Min. Sci. Technol.*, 2015, **25**, 219-223.
37. I. S. Kang and L. G. Leal, *Phys. Fluids*, 1988, **31**, 233-237.
38. F. Cappia, D. Pizzocri, M. Marchetti, A. Schubert, P. Van Uffelen, L. Luzzi, D. Papaioannou, R. Macian-Juan and V. V. Rondinella, *J. Nucl. Mater.*, 2016, **479**, 447-454.
39. K. D. N. Igata, *J. Nucl. Mater.*, 1972, **45**, 317-322.
40. W. K. Kim, J. H. Shim and M. Kaviani, *J. Nucl. Mater.*, 2017, **491**, 126-137.
41. L. E. Thomas, C. E. Beyer and L. A. Charlot, *J. Nucl. Mater.*, 1992, **188**, 80-89.
42. M. Tonks, D. Andersson, R. Devanathan, R. Dubourg, A. El-Azab, M. Freyss, F. Iglesias, K. Kulacsy, G. Pastore, S. R. Phillipot and M. Welland, *J. Nucl. Mater.*, 2018, **504**, 300-317.
43. F. Lemoine, *J. Nucl. Mater.*, 1997, **248**, 238-248.
44. F. Lemoine, Cadarache, 2000.
45. T. G. Lach, D. J. Edwards, E. C. Buck, B. K. McNamara, J. M.

- Schwantes and R. A. Clark, *J. Nucl. Mater.*, 2019, **521**, 120-125.
46. P. H. W. Dienst, D.K. Kerwin-Peck, *Nucl. Tech.*, 1984, **65**, 109-124.
47. C. A. Yablinsky, R. Devanathan, J. Pakarinen, J. Gan, D. Severin, C. Trautmann and T. R. Allen, *J. Mater. Res.*, 2015, **30**, 1473-1484.
48. P. M. Martin, E. Vathonne, G. Carlot, R. Delorme, C. Sabathier, M. Freyss, P. Garcia, M. Bertolus, P. Glatzel and O. Proux, *J. Nucl. Mater.*, 2015, **466**, 379-392.